Structures 62 (2024) 106101

Contents lists available at ScienceDirect

Structures

journal homepage: www.elsevier.com/locate/structures

Experimental and numerical evaluation of geometrical imperfection effects on the load bearing capacity of small-scaled voussoir arches

Davide Cassol [a], Giovanni Sommacal [a], Ivan Giongo [a], Gabriele Milani [b,*]

[a] Department of Civil, Environmental & Mechanical Engineering, University of Trento, Trento, Italy
[b] Department of Architecture, Built Environment and Construction Engineering, Politecnico of Milano, Milano, Italy

ARTICLE INFO

Keywords:
Masonry arches
Voussoirs
Geometrical imperfections
Linear programming
Plasticity theory

ABSTRACT

The study of the behaviour of masonry arches represents a complex problem, which involves different aspects that can significantly affect the load bearing capacity of such structures. In this regard, geometrical imperfections, such as the irregular shape of the arch blocks, the initial position of the first and last voussoirs (boundary conditions), the alignment between the adjoining blocks and the rounded corners of each block, play an important role. An experimental campaign was conducted on a toy arch made by eleven irregular blocks, with the aim of evaluating the effect of such irregularities. A numerical model was developed basing on lower bound (LB) and upper bound (UB) limit analysis approaches (referred to as the static and the kinematic theorem, respectively). A linear programming (LP) solving algorithm was implemented in the software MATLAB and used to solve the minimization/maximization problems. The probability distribution of each considered nonlinearity was estimated, the results of the numerical analysis were correlated with the experimental outcomes and a Montecarlo simulation was carried out to validate the hypothesised probability distributions.

1. Introduction

Masonry arches and vaults are largely diffused throughout Europe, especially in Italy. Such structures play an important role in historical constructions and monuments as well as in ordinary residential buildings, bridges and other infrastructures. The widespread use of masonry arches is due to their capability to cover large spans and carry relatively heavy gravity loads. Their structural efficiency is attributed to the curvature of the arch, which transfers vertical loads laterally along the curved structure to the abutments at each end. The curvature of the arch and the restraining provided by the abutments cause a combination of flexural stress and axial compression. The arch geometry can be manipulated to keep stresses primarily compressive [1], in order to take advantage of the good masonry compressive strength.

The following sets of equations provide useful tools for the structural analysis of masonry arches and vaults: i) equilibrium (statics), ii) geometry (compatibility) and iii) material (stresses). It is worth evidencing that in masonry voussoir arches, the stress level is typically much lower than that corresponding to the material failure, making the adoption of a simplified material behaviour quite convenient. Therefore, a stability or equilibrium approach carried out according to limit analysis procedures -usually specialized to no-tension materials-, appears as the natural choice to assess the safety of curved masonry structures in general [2–7] and of arches in particular [8–11]. Within Heyman's hypotheses, to apply classic limit analysis, three main assumptions should be adopted [12]: 1) masonry has no tensile strength, 2) it can resist infinite compression, and 3) sliding phenomena do not occur [13].

The limit analysis problem could be simplified using the infinitely resistant block method, adopted specifically for masonry structures and used by many authors for the determination of their collapse load [14–16]. Using this method, the structure is schematized as an assembly of infinitely resistant (and infinitely stiff) blocks and the problem's nonlinearity is concentrated at the interface of two adjacent blocks.

Equilibrium in a masonry arch could be visualized using the so-called line of thrust [17,18], a theoretical line representing the path of the resultants of the compressive forces throughout the arch. Structural stability is guaranteed when this line remains contained entirely within the section. The thrust line can also give information about possible collapse mechanisms. Structural curved elements exhibit failure modes caused by the formation of a sufficient number of flexural hinges, which arise where the thrust line touches the boundaries of the structure. Such considerations are helpful in particular for arches loaded in-plane.

* Corresponding author.
E-mail address: gabriele.milani@polimi.it (G. Milani).

https://doi.org/10.1016/j.istruc.2024.106101
Received 22 August 2023; Received in revised form 21 January 2024; Accepted 22 February 2024
Available online 7 March 2024
2352-0124/© 2024 The Author(s). Published by Elsevier Ltd on behalf of Institution of Structural Engineers. This is an open access article under the CC BY-NC-ND license (http://creativecommons.org/licenses/by-nc-nd/4.0/).

However, it is worth noting that a safety assessment can be provided using the line-of-thrust (or via limit analysis in general) not only for gravity and vertical point loads [19], but also for the in-plane static application of horizontal forces mimicking a seismic action [20]. For arches and bridges subjected especially to out-of-plane seismic excitation or when 3D out of plane effect cannot be disregarded, the analysis becomes more difficult and typically Finite or Distinct Elements are used [21–28], albeit very recently some extensions to the classic approach based on thrust lines have been proposed [29].

Despite the large diffusion of masonry arches and vaults, not all the aspects related to their structural behaviour are completely known. Even if the most probable failure mode corresponds to the formation of four hinges, the collapse of such masonry structural elements represents a complex problem, which involves many aspects, such as the role played by the infill [30,31], the geometry skewness, the slenderness, the presence of point loads, the imperfect shape of the voussoirs [32–34] (see Fig. 1) and the already existent state of damage [35,36].

These last two issues are critical and to some extent related one each other. As experimental and numerical literature show, indeed, they have a great influence in the decrease of the load bearing capacity and in the modification of the active failure mechanism [37].

In the present work, the theme of the influence of geometrical imperfection of both the voussoirs and the springing is analysed in detail, using classic lower and upper bound numerical approaches. As reference, a toy imperfect arch is considered. In particular, the results of a series of experimental tests carried out on a small-scale model of a masonry arch are reported and analysed. This experimental campaign was performed during the Summer School "*From Corbel Arches To Double Curvature Vaults: Data Acquisition, Structural Analysis, Conservation And Restoration Of Architectural Heritage Masonry*", which took place at Villa Grumello, Como Lake (Italy) in 2021 [40]. After the data acquisition, the arch model was schematized in the software MATLAB, and an upper and a lower bound limit analysis with infinitely resistant voussoirs were carried out to evaluate numerically the collapse load. Large scale Monte Carlo simulations were performed taking into account some geometric imperfections, which proved to affect considerably the behaviour of the real tested model at collapse.

2. Experimental campaign

A small-scale model of a masonry arch was hand built using eleven wood blocks (wood density of $842\ kg/m^3$) labelled from *1* to *11*, as illustrated in Fig. 2. Each block was realized by the union of five wood wedges with a radius of *60 mm*, a thickness of *12 mm* and a width of *50 mm*. The wedges were glued together to form a single block, which was later divided into two trapezoidal sections. The biggest one, with the global dimensions reported in Fig. 3, was used to construct the curved structure, after sandpaper was applied to the block-to-block contact surfaces in order to avoid sliding between contiguous voussoirs, as the blocks were stacked on top of each other dry. Such construction process of the single arch's unit was adopted to obtain blocks with the same average dimensions but characterized by an appreciable geometrical non-uniformity as typical of the existing arched structures.

After the construction of the eleven wood blocks, the arch was assembled trying to find the optimal stable configuration. The result was a structure with a span and a height of about *268 mm* and *81 mm*, respectively. The model was supported on two wedges covered with sandpaper, which ensured that sufficient static friction was transferred to the end blocks, as friction was the only mechanism keeping the blocks from sliding. Finally, two plastic springing separated the structure from the reaction floor. The construction phase was performed each time by a different experimenter. This was another way to increase the geometrical non-linearity that characterized the real existing arches.

After the construction phase, the structural stability and the correct disposition of the blocks were checked, and the resulting geometry was photographed. Then, the arch was incrementally loaded until the collapse by piling a series of fishing weights (weighing *5 g* each) in a small plastic bucket hanging from the structure. As can be seen in Fig. 2, the container was fixed to the structure by means of a lace connected to block *9*, applying a vertical concentrated load P_{exp}. After the collapse, the weights were counted and the value of P_{exp} was recorded. The container weight was not considered in the recorded value of P_{exp} because considered negligible (less than 5 g).

The test was repeated *28* times, collecting the results reported in Table 1. The arch collapsed with an ultimate load that ranged from *415* to *880 g*. It is important to notice the large scatter of the experimental

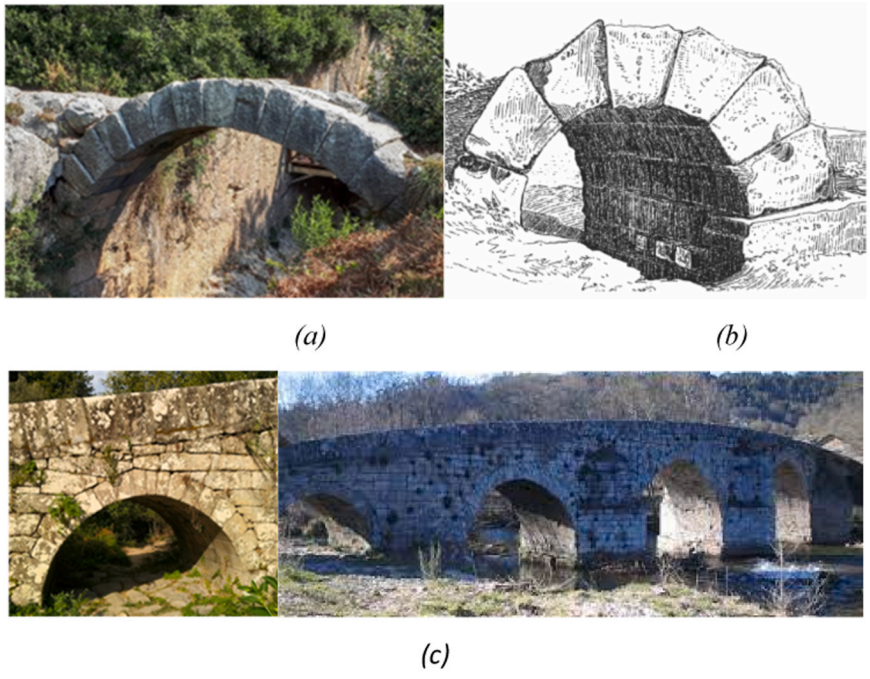

Fig. 1. Examples of stone arches with imperfect geometry of the voussoirs. (a) Titus tunnel bridge, Hatay, Turkey (b) Etruscan arch [38,39] (c) Cernadela Bridge, Spain.

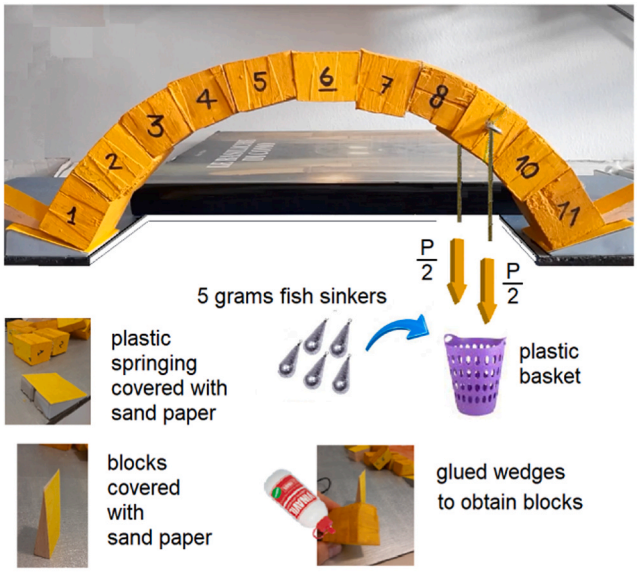

(a) Small-scaled set-up.

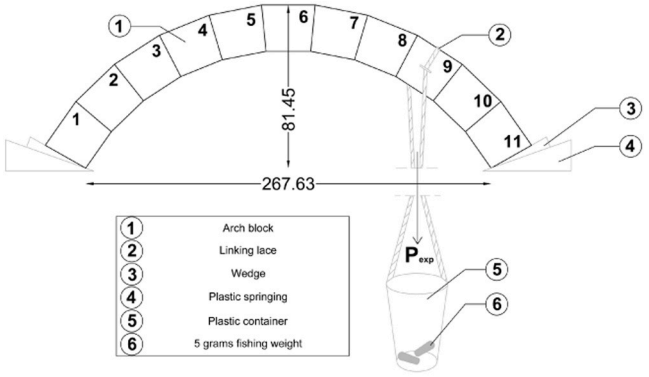

(b) Set-up scheme.

Fig. 2. Experimental test set up.

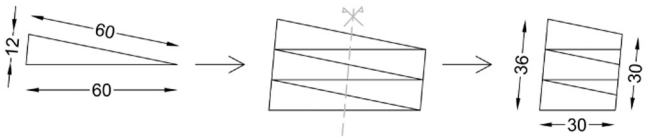

Fig. 3. Assembling process of the single arch block.

data, certainly related to the accuracy with which the structure was built. The average value of P_{exp} resulted equal to *542.7 g* (COV_{Pexp}=*0.19*). Specifically, the authors performed three tests, namely A01, A02 and A03, obtaining three values of P_{exp} equal to *545*, *590* and *535 g*, respectively.

During the loading application, the evolution of each failure mechanism was monitored by taking videos. Fig. 4 illustrates an example of collapse. A four-hinges mechanism was observed: a failure mode that is typical for full-scale unreinforced masonry arches.

Table 1
Experimental results in terms of vertical load P_{exp} [grams].

ID	P_{exp} [*grams*]	ID	P_{exp} [*grams*]
A01	**545**	A15	445
A02	**590**	A16	560
A03	**535**	A17	515
A04	575	A18	495
A05	485	A19	560
A06	435	A20	485
A07	585	A21	580
A08	625	A22	440
A09	880	A23	415
A10	485	A24	475
A11	595	A25	540
A12	640	A26	765
A13	580	A27	445
A14	490	A28	430

Mean μ_{Pexp}= 542.7 g; Standard Deviation σ_{Pexp} = 102.1 g.

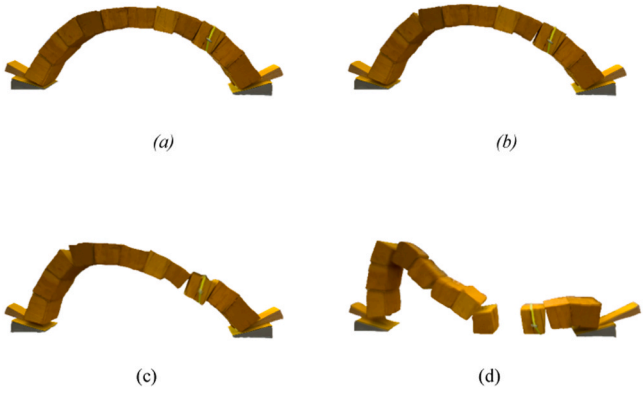

Fig. 4. Evolution of the experimental failure mode.

3. Numerical model

After the experimental phase, a numerical model based on the limit analysis theorems was created using the software MATLAB [41]. Two different numerical approaches were adopted: the lower bound (LB) approach which uses the static theorem and the upper bound (UB) approach which is based on the kinematic theorem [42]. The minimization/maximization problem was solved using the linear programming solving algorithm implemented by default in MATLAB [43–45]. The two approaches should bring to the same solution and consequently it is possible to check if the two models are correctly implemented by means of a comparison between the obtained outcomes.

3.1. Lower Bound Linear Programming (LBLP) approach

The LBLP approach relies on the static theorem. All the possible solutions were evaluated under the hypothesis that each block must remain in equilibrium and that the internal actions on the interfaces must not violate the strength domain (i.e., the thrust line lies within the arch profile). The maximum collapse multiplier λ_{ST} was calculated using a linear programming algorithm. Fig. 5 shows the forces acting on the block *k* and the interfaces *i*, *i-1* of the arch. Each interface between contiguous blocks *k* and $k + 1$ exchanges a normal force N_i, a shear force V_i and a bending moment M_i. The loads acting on each block *k* are the vertical load W_k, the horizontal load H_k and the bending moment M_k.

The equilibrium equations for each block in the horizontal, vertical ad rotational directions can be written in a matrix form as in Eqs. 1 and 2. The matrix G_k allows correlating the internal actions of the interface *i* and *i-1* applied to the centroid of the interface (vectors X_i and X_{i-1}) with the external loads (vector F_k) and the loads dependent by the collapse

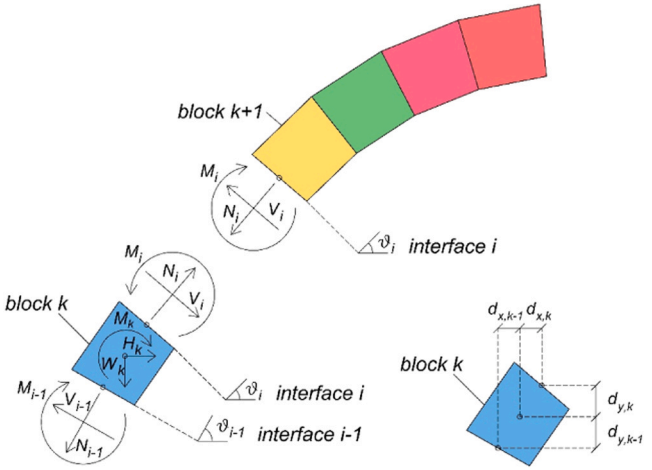

Fig. 5. Forces acting on blocks and interfaces.

multiplier λ (vector $F_{\lambda,k}$) which act on the centroid of the block k. The static admissibility condition was imposed on each interface as indicated in Eqs. 3 and 4, where t is the thickness of the interface i.

$$\begin{bmatrix} \cos(\vartheta_{i-1}) & \sin(\vartheta_{i-1}) & 0 & \cos(\vartheta_i) & \sin(\vartheta_i) & 0 \\ \sin(\vartheta_{i-1}) & \cos(\vartheta_{i-1}) & 0 & \sin(\vartheta_i) & \cos(\vartheta_i) & 0 \\ a & b & -1 & c & d & 1 \end{bmatrix} \bullet \begin{bmatrix} N_{i-1} \\ V_{i-1} \\ M_i - 1 \\ N_i \\ V_i \\ M_i \end{bmatrix}$$

$$= \begin{bmatrix} H_k \\ W_k \\ M_k \end{bmatrix} + \begin{bmatrix} H_{\lambda,k} \\ W_{\lambda,k} \\ M_{\lambda,k} \end{bmatrix}$$

where :

$$a = d_{x,k-1}\sin(\vartheta_{i-1}) - d_{y,k-1}\cos(\vartheta_{i-1})$$

$$b = -d_{x,k-1}\cos(\vartheta_{i-1}) - d_{y,k-1}\sin(\vartheta_{i-1})$$

$$c = d_{x,k}\sin(\vartheta_i) - d_{y,k}\cos(\vartheta_i)$$

$$d = -d_{x,k}\cos(\vartheta_i) - d_{y,k}\sin(\vartheta_i) \quad (1)$$

$$G_k \begin{bmatrix} X_{i-1} \\ X_i \end{bmatrix} = F_k + F_{\lambda,k} \quad (2)$$

$$\begin{bmatrix} \frac{t_i}{2} & 0 & 1 \\ \frac{t_i}{2} & 0 & -1 \end{bmatrix} \begin{bmatrix} N_i \\ V_i \\ M_i \end{bmatrix} \le \begin{bmatrix} 0 \\ 0 \end{bmatrix} \quad (3)$$

$$G_{\text{int},i} X_i \le b_{\text{int},i} \quad (4)$$

The LBLP problem can be written as indicated in Eqs. 5 and 6, where the matrixes G_{abs} and $G_{abs,in}$ and the vectors $F_{abs,w}$, F_{abs} and $b_{abs,in}$ can be obtained assembling the matrixes indicated in Eqs. 1 and 2 (see Eqs. 7–11). The maximum collapse multiplier λ_{ST} and the corresponding vector of the internal actions X ($3ni \times 1$) can be solved using the linear programming approach. The results can be visualized by means of the line of trust which is determined by calculating the eccentricity e_i of the axial load in every interface i as indicated in Eq. 12.

$$\max(\lambda)$$

$$\begin{cases} G_{abs} X = F_{abs,W} + F_{abs,\lambda} \\ G_{abs,in} X \le b_{abs,in} \end{cases} \quad (5)$$

$$\max\left(\begin{bmatrix} 0_{1*3Ni} & 1 \end{bmatrix} \begin{bmatrix} X \\ \lambda \end{bmatrix} \right)$$

$$\begin{cases} \begin{bmatrix} G_{abs} & -F_{abs,\lambda} \end{bmatrix} \begin{bmatrix} X \\ \lambda \end{bmatrix} = F_{abs,W} \\ \begin{bmatrix} G_{abs,in} & 0_{2Ni*1} \end{bmatrix} \begin{bmatrix} X \\ \lambda \end{bmatrix} \le b_{abs,in} \end{cases} \quad (6)$$

$$G_{abs} = \begin{bmatrix} G_{k=1} & 0 & \cdots & 0 \\ 0 & G_{k=2} & \ddots & \vdots \\ \vdots & \ddots & \ddots & 0 \\ 0 & \cdots & 0 & G_{k=nb} \end{bmatrix} (3nb \times 3ni) \quad (7)$$

$$G_{abs,in} = \begin{bmatrix} G_{\text{int},i=1} & 0 & \cdots & 0 \\ 0 & G_{\text{int},i=2} & \ddots & \vdots \\ \vdots & \ddots & \ddots & 0 \\ 0 & \cdots & 0 & G_{\text{int},i=ni} \end{bmatrix} (2ni \times 3ni) \quad (8)$$

$$F_{abs} = \begin{bmatrix} F_{k=1} \\ F_{k=2} \\ \vdots \\ F_{k=nb} \end{bmatrix} (3nb \times 1) \quad (9)$$

$$F_{\lambda,abs} = \begin{bmatrix} F_{\lambda,k=1} \\ F_{\lambda,k=2} \\ \vdots \\ F_{\lambda,k=nb} \end{bmatrix} (3nb \times 1) \quad (10)$$

$$b_{abs,in} = \begin{bmatrix} b_{\text{int},i=1} \\ b_{\text{int},i=2} \\ \vdots \\ b_{\text{int},i=ni} \end{bmatrix} (2nib \times 1) \quad (11)$$

$$e_i = \frac{M_i}{N_i} \quad (12)$$

3.2. Upper bound linear programming (UBLP) approach

The UBLP approach is based on the use of the kinematic theorem. All the possible solutions were evaluated by considering that there is no interpenetration nor sliding between contiguous blocks. The minimum collapse multiplier λ_{KIN} was calculated using a linear programming algorithm. Fig. 6 shows the velocities of the nodes of the blocks k, $k+1$ and the interface i of the arch. For each block three independent variables can be identified (vector Y_k): the velocity of the block in the

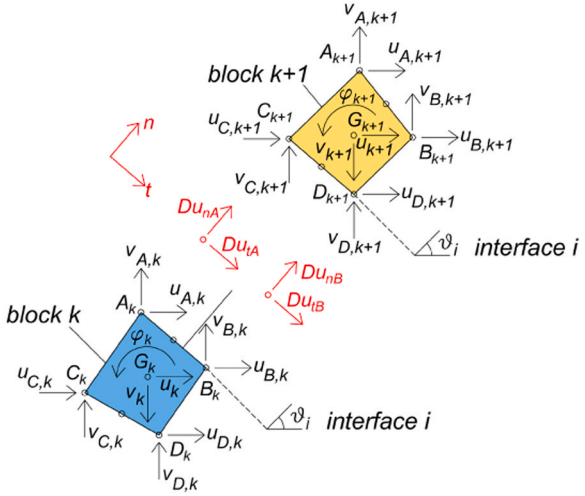

Fig. 6. Block velocities.

horizontal direction u_k, the velocity of the block in the vertical direction v_k and the rotation speed rate around the centroid φ_k.

The horizontal and vertical velocities of the four vertices of each block k (points A_k, B_k, C_k and D_k) can be determined as a function of u_k, v_k and φ_k and considering the geometry of the block. Eqs. 13 and 14 report an example of the calculation of the velocities of the nodes A and C of the blocks k and $k+1$, in order to introduce the adopted notation of the correlation matrixes $G_{A,k}$ and $G_{C,K+1}$. The compatibility equations for each interface can be written in matrix form as two inequalities and two equalities: Eq. 15 represents the condition of no interpenetration of the nodes (positive difference of velocities in the direction normal to the interface n $D_{un,k}$), while Eq. 16 reports the assumption of no sliding (no difference of velocities in the direction parallel to the interface t $D_{ut,k}$).

$$u_{A,k+1} = n^T \begin{bmatrix} u_{A,k+1} \\ v_{A,k+1} \end{bmatrix} = n^T \begin{bmatrix} 1 & 0 & -\left(y_{A,k} - y_{G,k}\right) \\ 0 & 1 & \left(x_{A,k} - x_{G,k}\right) \end{bmatrix} \begin{bmatrix} u_1 \\ v_k \\ \varphi_k \end{bmatrix} = n^T \cdot G_{A,k} Y_k \tag{13}$$

$$u_{C,k+1} = n^T \begin{bmatrix} u_{C,k+1} \\ v_{C,k+1} \end{bmatrix} = n^T \begin{bmatrix} 1 & 0 & -\left(y_{C,k+1} - y_{G,k+1}\right) \\ 0 & 1 & \left(x_{C,k+1} - x_{G,k+1}\right) \end{bmatrix} \begin{bmatrix} u_{k+1} \\ v_{k+1} \\ \varphi_{k+1} \end{bmatrix} = n^T \cdot G_{C,k+1} \cdot Y_{k+1} \tag{14}$$

$$\begin{bmatrix} D_{u_n A,k} \\ D_{u_n B,k} \end{bmatrix} = \begin{bmatrix} n & n \end{bmatrix}^T \begin{bmatrix} - & G_{A,k} & G_{C,k+1} \\ - & G_{B,k} & G_{D,k+1} \end{bmatrix} \begin{bmatrix} Y_k \\ Y_{k+1} \end{bmatrix} \geq 0 \tag{15}$$

$$\begin{bmatrix} D_{u_t A,k} \\ D_{u_t B,k} \end{bmatrix} = \begin{bmatrix} t & t \end{bmatrix}^T \begin{bmatrix} - & G_{A,k} & G_{C,k+1} \\ - & G_{B,k} & G_{D,k+1} \end{bmatrix} \begin{bmatrix} Y_k \\ Y_{k+1} \end{bmatrix} = 0 \tag{16}$$

$$where: n = \begin{bmatrix} \cos(\vartheta_i) \\ \sin(\vartheta_i) \end{bmatrix}; t = \begin{bmatrix} \sin(\vartheta_i) \\ -\cos(\vartheta_i) \end{bmatrix};$$

The UBLP problem is reported in Eqs. 17 and 18, where the matrixes $A_{eq,ass}$ and $A_{ass,in}$ and the vector W_0 can be obtained assembling the matrixes indicated in the Eqs. 15 and 16 (see Eqs. 19–22). The minimum collapse multiplier λ_{KIN} and the corresponding vector of the block velocities Y ($3ni \times 1$) can be solved using the linear programming approach. The LP problem is normalized defining the power expended by the collapse multiplier equal to one when the collapse multiplier P_1 is set unitary. The results can be visualized by plotting the collapse mechanism, which is known up to a magnification factor.

$$\min(\lambda) \quad \begin{cases} A_{eq,ass} Y = 0_{2Ni*1} \\ P_1 Y = 1 \\ A_{in,ass} Y \geq 0_{2Ni*1} \end{cases} \tag{17}$$

$$\min(-W_0 Y) \quad \begin{cases} A_{eq,ass} Y = 0_{2Ni*1} \\ P_1 Y = 1 \\ A_{in,ass} Y \geq 0_{2Ni*1} \end{cases} \tag{18}$$

$$A_{in,ass} = \begin{bmatrix} D_{u_n A,k=1} & 0 & \cdots & 0 \\ D_{u_n B,k=1} & D_{u_n A,k=2} & \ddots & \vdots \\ 0 & D_{u_n B,k=2} & \ddots & 0 \\ \vdots & \ddots & \ddots & D_{u_n A,k=nb} \\ 0 & \cdots & 0 & D_{u_n B,k=nb} \end{bmatrix} (2ni \times 3nb) \tag{19}$$

$$A_{eq,ass} = \begin{bmatrix} D_{u_t A,k=1} & 0 & \cdots & 0 \\ D_{u_t B,k=1} & D_{u_t A,k=2} & \ddots & \vdots \\ 0 & D_{u_t B,k=2} & \ddots & 0 \\ \vdots & \ddots & \ddots & D_{u_t A,k=nb} \\ 0 & \cdots & 0 & D_{u_t B,k=nb} \end{bmatrix} (2ni \times 3nb) \tag{20}$$

$$W_0 = \begin{bmatrix} W_{k=1} & W_{k=2} & \cdots & W_{k=nb} \end{bmatrix} (3nb \times 1) \tag{21}$$

$$P_1 = \begin{bmatrix} 0 & 0 & P_{1,k=3} = (0-10) & 0 & \cdots & 0 \end{bmatrix} (3nb \times 1) \tag{22}$$

4. Numerical Analyses

4.1. Regular configuration

The numerical model was initially used to study the behaviour of an arch constructed with regular blocks (block lengths at the extrados, intrados and interface equal to *36 mm*, *30 mm* and *30 mm*, respectively) with the final dimensions reported in Fig. 3. The results of the analysis reported in Fig. 7, shows the collapse mechanism and the line of trust obtained using the kinematic (UBLP) and static (LBLP) approaches. The obtained value of the collapse load ($P_{exp} = 895.6$ *g*) is noticeably higher than the average load obtained experimentally ($\mu_{Pnum} = 542.7$ *g; COV-*$_{Pnum}$ *= 0.19),* and also higher than the maximum measured value (*880 g*). As expected, the geometric nonlinearity considerably affected the load bearing capacity of the analysed arch, with a mean reduction of the collapse load of *55%*.

4.2. Imperfections of the block geometry

In this work, four types of geometrical nonlinearities were considered: the irregular shape of the arch blocks, the initial position of the first element, the alignment between the adjoining blocks and the rounded corners of each block.

4.2.1. Irregular shape of the arch blocks

Photo rectifications of the pictures of the unloaded models A01, A02 and A03 were performed with the software RDF [46]. The measured length of the span and the raise were used as reference to define the shape of the arch. Each block was represented by four points, corresponding to the four edges of the unit. In this way, models A01, A02 and A03 could be correctly drawn and imported in MATLAB as places of points in the *xy* plane. In the model, the contact surfaces between the voussoirs were assumed to be flat and the effect of possible small surface unevenness were neglected. Such approximation is compatible with the response of the tested arch. Once the arch approached its maximum load-bearing capacity, in fact, the failure mechanism starts activating with small rotations of the critical voussoirs. As such rotations develop, contact points at the voussoir interfaces shift to the edges of the block independently from the presence of irregularities on the interface. After the assembly phase, the boundary conditions and the interface properties of the arch were assigned, following either the LBLP or the UBLP approach, as detailed in *Section 3* . Fig. 8 displays the corrected photo and the geometry imported into *MATLAB* for model *A02*. As depicted in Fig. 9, the irregular shape of the arch blocks was quantified using three different parameters: the length at the extrados l ($\mu_l = 36.1$ *mm;* $COV_l = 0.09$), the planar area A ($\mu_A = 975$ *mm*^{2}*;* $COV_A = 0.11$) and the angle between the interfaces α ($\mu_\alpha = 11.6°$*;* $COV_\alpha = 0.13$).

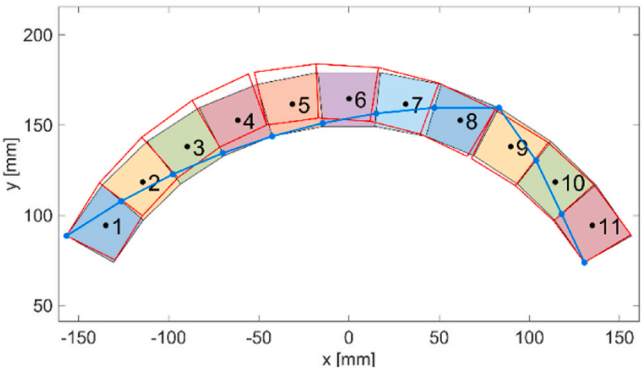

Fig. 7. Standard configuration results (P_{exp}=895.6 g).

(a) Photo rectification of model A02.

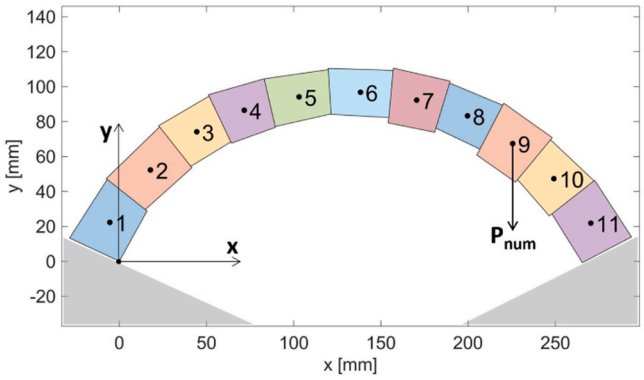

(b) Scheme of model A02 extracted from MATLAB.

Fig. 8. Example of photo rectification of the arch.

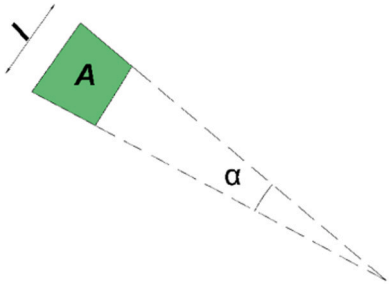

Fig. 9. Definition of the irregular shape of the arch blocks.

4.2.2. Initial position of the first element

The initial interface angle of block 1 was considered as a variable due to the different positions of the wedge inserted between block 1 and the plastic springing. As shown in Fig. 10, a mean value equal to *25.5°* was estimated for this parameter and a normal distribution with a standard deviation of *2.5°* was assigned to the interface angle. Such values of mean and standard deviation were calibrated in accordance with the experimental values measured by means of photo rectification.

4.2.3. Alignment between the adjoining voussoirs

The arch blocks were not perfectly aligned due to their different shape and the positioning errors arising during construction. The extrados corner was considered as reference for the blocks alignment, exactly as it was done in the construction stage. A normal distribution, with a mean value and a standard deviation of *0 mm* and *2.5 mm*, respectively, was assumed for the positioning of the blocks, as reported in Fig. 11. Such values were defined in accordance with the experimental outcomes.

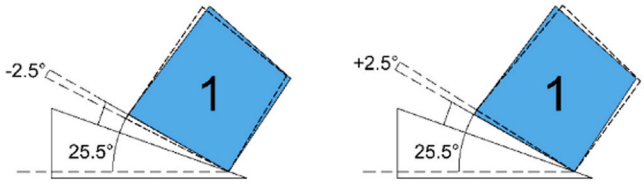

Fig. 10. Initial position of the first element.

4.2.4. Rounded corners of each block

The blocks used in the small-scaled arch were characterized by rounded corners, which were consequently considered in the model. Fig. 12 depicts how the interface length corresponding to each corner was reduced of *1.3 mm* to account such imperfections. This nonlinearity was due to the construction phase previously illustrated (Fig. 3) and, therefore, a constant value was assigned to all the blocks corners.

4.3. Model validation

The behaviour of the arch specimens A01, A02 and A03 were analysed and the obtained numerical outcomes were compared with the experimental ones (see Fig. 13, Fig. 14 and Fig. 15). For each experimental test, the arch geometry and the block positions were detected from the photo rectification, while the rounded block corners were considered as previously described.

The numerical models provided results consistent with the experimental evidence, with the collapse load of the three specimens being accurately estimated. The percent deviation was in fact equal to *-0.28%, 0.34%,* and *-0.48%* for model A01, A02, and A03, respectively. Such a level of accuracy was reached despite the minimum weight increment during testing being equal to *5 g*. In addition, for each arch, the numerical model was able to capture the failure mode observed experimentally.

4.4. Montecarlo simulation

Once the geometrical non-linearities had been considered, a statistical analysis (Montecarlo simulation) was performed, as illustrated in Fig. 16. The correct geometry and the corner rounding of the blocks experimentally measured were used in the simulations. Ten-thousand arch specimens were generated, compatibly with the above-described probability distribution of the initial position of the first element and the alignment between each adjoining block. The analysis was performed using a *16 Gb* RAM computer, with a total computational time equal to *32 min*. Fig. 17 reports the resulting histogram and the curves of the normal probability distribution obtained both numerically (μ_{Pnum} = *544.3 g;* COV_{Pnum} = *0.19*) and experimentally (μ_{Pexp} = *542.7 g;* COV_{Pexp} = *0.19*). The numerical results appeared consistent with the experimental data, with a percent deviation smaller than *0.57%*, suggesting that the considered probability distribution of the geometrical non-linearities had been properly calibrated.

Among the ten-thousand models, the arch configurations that lead to the largest and the smallest collapse loads are reported in Fig. 18. It can be noticed how the geometrical non-linearities considerably affected the ultimate load and the relative failure mode by varying the value of the collapse load up to *87%* from the average value. As expected, the range between the minimum and maximum values of the collapse load obtained from the simulation contained all the experimental values reported in Table 1 due to the different number of analysed configurations.

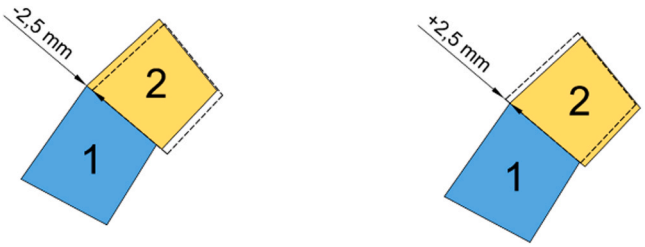

Fig. 11. Alignment between the adjoining blocks.

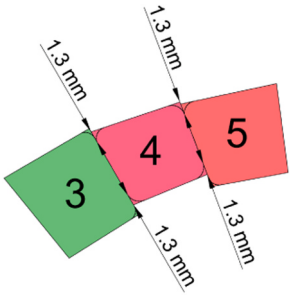

Fig. 12. Rounded corners of each block.

(a) Experimental outcomes (P_{exp}=545 grams).

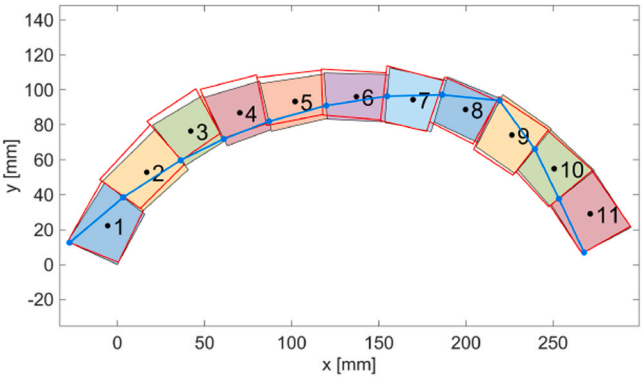

(b) Numerical outcomes (P_{num}=543.5 grams).

Fig. 13. Results of the specimen A01.

5. Conclusions

An experimental campaign was conducted with the aim of evaluating the effect of the geometrical non-linearities on the load bearing capacity of a small-scale arch, made of eleven irregular voussoirs. With such purpose, a numerical analysis was performed using the software MATLAB, considering as geometrical non-linearities the irregular shape of the arch blocks, the initial position of the first element, the alignment between the adjoining blocks and the rounded corners of each block. The following conclusions were drawn:

- When assessing real full-scale arched structures, it is quite common to refer to an idealized geometry characterized by identical voussoirs. The results presented herein show, albeit with reference to a small-scale toy arch, that an accurate geometric survey is critical to a correct assessment of the load-carrying capacity of voussoir arches.
- The outcomes of twenty-eight tests performed on the small-scaled arch specimens were collected. The measured collapse load values (μ_{Pexp} = *542.7 g; COV*$_{Pexp}$= *0.19*) showed that the geometrical non-linearities considerably influenced the response of the arch, suggesting how such non-linearities should be considered when analysing curved structures.

(a) Experimental outcomes (P_{exp}=590 grams).

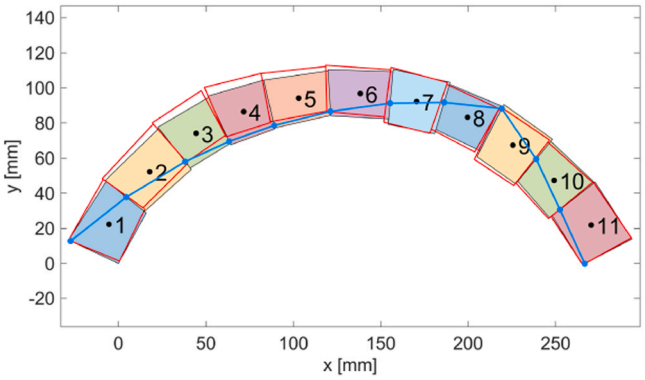

(b) Numerical outcomes (P_{num}=592.0 grams).

Fig. 14. Results of the specimen A02.

(a) Experimental outcomes (P_{exp}=535 grams).

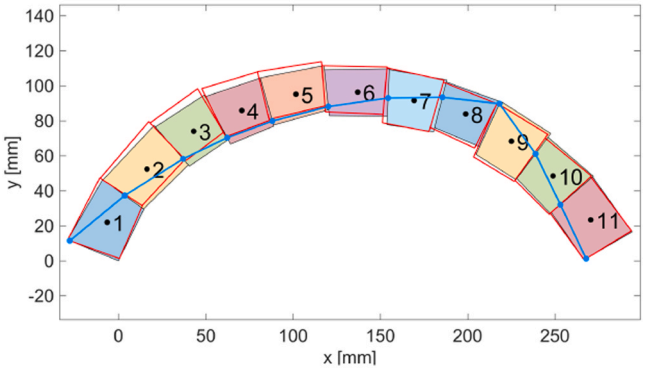

(b) Numerical outcomes (P_{num}=532.4 grams).

Fig. 15. Results of the specimen A03.

- A numerical model, based on limit analysis theorems, was developed and validated on the experimental data both in terms of ultimate load and failure mode. Two numerical approaches were used: the lower bound (LB) and the upper bound (UB) approach which are referred to the static and the kinematic theorem, respectively. The minimization/maximization problem was solved with a linear programming solving algorithm.
- A non-negligible difference between the failure load values of the regular and the irregular configurations was noticed, leading to a

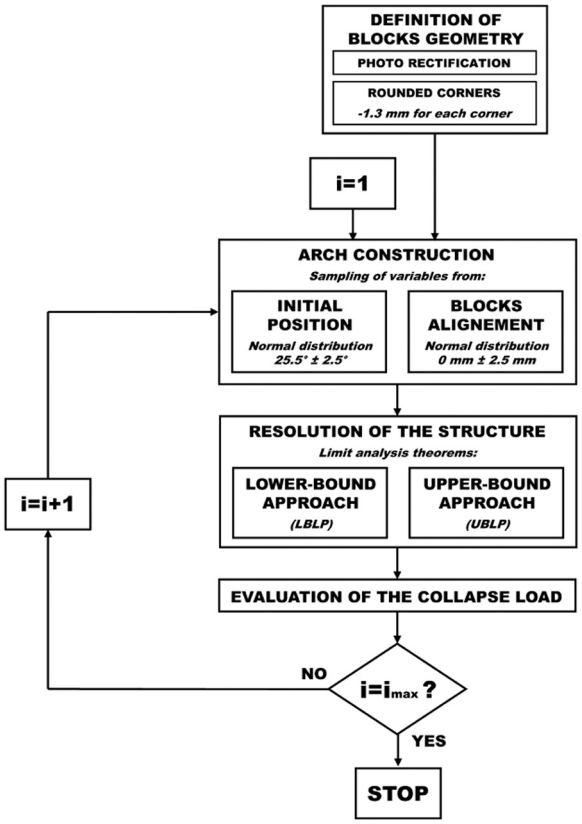

Fig. 16. Montecarlo simulation flow chart.

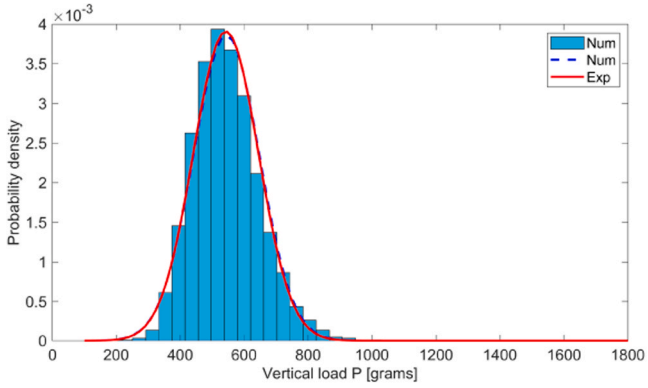

Fig. 17. Montecarlo simulation results (μ_{Pnum} = 544.3 g; COV_{Pnum} = 0.19).

reduction of *55%* of the load-bearing capacity due to the presence of irregularities.

- The main geometrical-nonlinearities which could affect the behaviour of the tested small-scaled structure were identified and their probability distributions were estimated according to the experimental results.
- Among the twenty-eight performed tests, three selected configurations of blocks were analysed in detail (with their real geometry) to validate the numerical model.The probability distribution of geometrical nonlinearities involved in the problem was validated by means of a Montecarlo simulation, generating additional ten-thousand arch configurations. The obtained numerical probability distribution resulted to be consistent with the experimental outcomes.

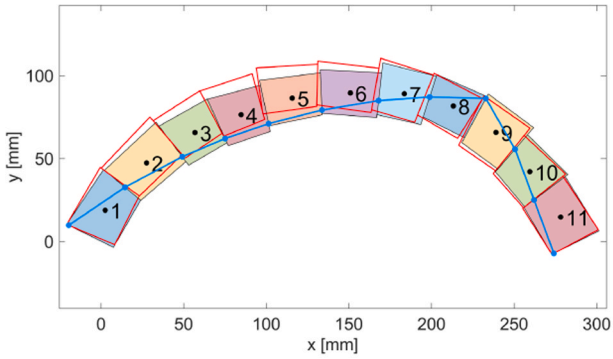

(a) Numerical configuration with the maximum collapse load (P_{num}=1022.1 grams).

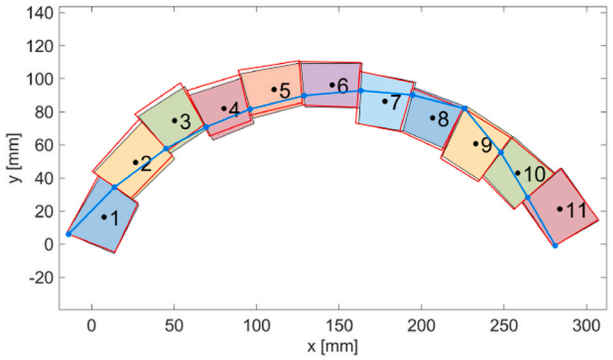

(b) Numerical configuration with the minimum collapse load (P_{num}=257.3 grams).

Fig. 18. Configurations obtained from the Montecarlo simulation with the maximum and the minimum collapse load.

Declaration of Competing Interest

The authors declare that they have no known competing financial interests or personal relationships that could have appeared to influence the work reported in this paper.

Acknowledgements

The authors acknowledge the Italian Ministry of Universities and Research (MUR), in the framework of the project DICAM-EXC (Departments of Excellence 2023–2027, grant L232/2016).

Gabriele Milani gratefully acknowledges the Italian Ministry of Foreign Affairs (research project 2022-2024 MAECI, grant CUP D23C22000060006) and the Department of Science and Technology (International Corporation Division), India, grant INT/Italy/P- 29/2022. He also gratefully acknowledges the 2022-2024 ReLUIS Project—WP10 Masonry Structures (Coordinator—Guido Magenes), funded by the Italian Department of Civil Protection.

References

[1] Kimura T, Ohsaki M, Fujita S, Michiels T, Adriaenssens S. Shape optimization of no-tension arches subjected to in-plane loading. Structures 2020;28:158–69. https://doi.org/10.1016/j.istruc.2020.08.053. ⟨https://www.scopus.com/inward/record.uri?eid=2-s2.0-5090117060&doi=10.1016%2fj.istruc.2020.08.053&partnerID=40&md5=9ae871acb5f9ac3fccf269cad4f88dba⟩.

[2] O'Dwyer D. Funicular analysis of masonry vaults. Comput Struct 1999;73(1-5):187–97.

[3] Block P. *Real-time limit analy-sis of vaulted masonry buildings*. Comput Struct 2006; vol. 84(29-30):1841–52.

[4] Block p, Ochserdorf JA. Thrust network analysis: a new methodology for three-dimensional equilibrium. J IASS 2007;vol. 48(3):167–73.

[5] Fraternali FA. Thrust network approach for the equilibrium problem of unreinforced masonry vaults via polyhedral stress functions. Mech Res Commun 2010;37(2):198–204.
[6] Marmo F, Masi D, Mase D, Rosati L. Thrust network analysis of masonry vaults. Int J Mason Res Innov 2019;4(1-2):64–77.
[7] Marmo F, Rosati L. Reformulation and extension of the thrust network analysis. Comput Struc 2017;182:104–18.
[8] Nodargi NA, Bisegna P. Thrust line analysis revisited and applied to optimization of masonry arches. Int J Mech Sci 2020;179:105690.
[9] Kooharian A. Limit analysis of voussoir (segmental) and concrete arches. J Am Concr Inst 1952;24(4):317–28.
[10] Livesley RK. Limit analysis of structures formed from rigid blocks. Int J Num Methods Eng 1978;vol. 12:1853–71.
[11] Stockdale G, Tiberti S, Camilletti D, Sferrazza Papa G, Basshofi, Habieb A, et al. Kinematic collapse load calculator: circular arches. SoftwareX 2018;7:174–9. https://doi.org/10.1016/j.softx.2018.05.006.
[12] Heyman J. The stone skeleton. Int J Solids Struct 1966;vol. 2(2):265–79.
[13] Hua, Y., Milani, G. Simple modelling of reinforced masonry arches for associated and non-associated heterogeneous limit analysis (2023) Computers and Structures, 280, art. no. 106987. https://www.scopus.com/inward/record.uri?eid=2-s2.0–85147545013&doi=10.1016%2fj.compstruc.2023.106987&partnerID=40&md5=962e000fbffa09b1190a23d022838e6d.
[14] Gilbert M. and Melbourne, C. *Rigid-block analysis of masonry structures*. Struct Eng 1994;vol. 72(21):356–61.
[15] Baggio C, Trovalusci P. Collapse behaviour of three-dimensional brick-block systems using non-linear programming. Struct Eng Mech 2000;vol. 10(2):181–95.
[16] Ferris M, Tin-Loi F. Limit analysis of frictional block assemblies as a mathematical program with complementarity constraints. Int J Mech Sci 2001;vol. 43(1):209–24.
[17] Méry, E. Sur l'équilibre des voûtes en berceau Annales des Ponts et Chaussées, vol. 19, pp. 50–70, 1840.
[18] Moseley H. The Mechanical Principles of Engineering and Architecture. London: Longman, Brown, Green and Longmans; 1843.
[19] Chiozzi, A., Malagù, M., Tralli, A., and Cazzani, A. ArchNURBS: NURBS-Based Tool for the Structural Safety Assessment of Masonry Arches in MATLAB. Journal of Computing in Civil Engineering Volume 30, Issue 2 https://doi.org/10.1061/(ASCE)CP.1943–5487.0000481.
[20] Marmo F. Archlab: A MATLAB tool for the Thrust Line Analysis of masonry arches. Curved Layer Struct 2021;8(1):26–35. https://doi.org/10.1515/cls-2021-0003. ⟨https://www.scopus.com/inward/record.uri?eid=2-s2.0-85101553000&doi=10.1515%2fcls-2021-0003&partnerID=40&md5=adc9dee1df799d1c61d14e48620ba6c5⟩.
[21] Zampieri P, Tetougueni CD, Pellegrino C. Nonlinear seismic analysis of masonry bridges under multiple geometric and material considerations: application to an existing seven-span arch bridge. Structures 2021;34:78–94. https://doi.org/10.1016/j.istruc.2021.07.009. ⟨https://www.scopus.com/inward/record.uri?eid=2-s2.0-85111281318&doi=10.1016%2fj.istruc.2021.07.009&partnerID=40&md5=efe94320a0a3c69bb753ee843cd15991⟩.
[22] Saygılı Ö, Lemos JV. Seismic vulnerability assessment of masonry arch bridges. Structures 2021;33:3311–23. https://doi.org/10.1016/j.istruc.2021.06.057. ⟨https://www.scopus.com/inward/record.uri?eid=2-s2.0-85108867870&doi=10.1016%2fj.istruc.2021.06.057&partnerID=40&md5=f6d6c78bb4477182ac723dbfe570c4c6⟩.
[23] Milani G, Lourenco PB. 3D non-linear behavior of masonry arch bridges. Comput Struct 2012;110:133–50.
[24] Mahmoudi P, Asadi P, Eftekhar MR. The effect of geometric dimensions on the lateral bearing capacity of the masonry arches. Structures 2022;45:1350–65. https://doi.org/10.1016/j.istruc.2022.09.059. ⟨https://www.scopus.com/inward/record.uri?eid=2-s2.0-85139322500&doi=10.1016%2fj.istruc.2022.09.059&partnerID=40&md5=b8cd77876944cc5c19171217437df2e1⟩.
[25] Silva, R., Costa, C., Arêde, A. Numerical methodologies for the analysis of stone arch bridges with damage under railway loading (2022) Structures, 39, pp. 573–592. https://www.scopus.com/inward/record.uri?eid=2-s2.0–85127070167&doi=10.1016%2fj.istruc.2022.03.063&partnerID=40&md5=94f9efd32ad20d73b0ea1e17ea17b99f DOI: 10.1016/j.istruc.2022.03.063.
[26] Hejazi M, Mehdian A. Experimental and numerical investigation on masonry arch bridges under uniform and line loads. Structures 2023;47:665–80. https://doi.org/10.1016/j.istruc.2022.11.101. ⟨https://www.scopus.com/inward/record.uri?eid=2-s2.0-85143510495&doi=10.1016%2fj.istruc.2022.11.101&partnerID=40&md5=b6661c4069bf4875bde309e8ba4d244b⟩.
[27] Sarhosis V, Forgács T, Lemos JV. A discrete approach for modelling backfill material in masonry arch bridges. Comput Struct 2019;224:106108.
[28] Tóth AR, Orbán Z, Bagi K. Discrete element analysis of a stone masonry arch. Mech Res Commun 2009;36(4):469–80.
[29] Grillanda N, Chiozzi A, Milani G, Tralli A. NURBS solid modeling for the three-dimensional limit analysis of curved rigid block structures. Comput Methods Appl Mech Eng 2022;399:115304. https://doi.org/10.1016/j.cma.2022.115304.
[30] Sarhosis, V., Forgács, T., Lemos, J.V. A discrete approach for modelling backfill material in masonry arch bridges (2019) Computers and Structures, 224, art. no. 106108. https://www.scopus.com/inward/record.uri?eid=2-s2.0–85071472417&doi=10.1016%2fj.compstruc.2019.106108&partnerID=40&md5=a898039f62443f8aa7c1cfb7c03b71fc.
[31] Papa, T., Grillanda, N., Milani, G. Three-dimensional adaptive limit analysis of masonry arch bridges interacting with the backfill (2021) Engineering Structures, 248, art. no. 113189. https://www.scopus.com/inward/record.uri?eid=2-s2.0–85115753537&doi=10.1016%2fj.engstruct.2021.113189&partnerID= [?tjl]?>;40&md5=1506e15f094a9d6c4e503831c6d7c79b DOI: 10.1016/j.engstruct.2021.113189.
[32] Cavalagli N, Gusella V, Liberotti R. Effect of shape uncertainties on the collapse condition of the circular masonry arch. Adv Struct Mater 2020;130:455–67. https://doi.org/10.1007/978-3-030-50460-1_27. ⟨https://www.scopus.com/inward/record.uri?eid=2-s2.0-85090513436&doi=10.1007%2f978-3-030-50460-1_27&partnerID=40&md5=56a455f75ac93dd9f0a0a3c8436a0248⟩.
[33] Cavalagli N, Gusella V, Liberotti R. The role of shape irregularities on the lateral loads bearing capacity of circular masonry arches. Lect Notes Mech Eng 2020:2069–81. https://doi.org/10.1007/978-3-030-41057-5_164. ⟨https://www.scopus.com/inward/record.uri?eid=2-s2.0-85083969824&doi=10.1007%2f978-3-030-41057-5_164&partnerID=40&md5=da9290b54d6e2e428c5eed9a84ea42dd⟩.
[34] Severini L, Cavalagli N, DeJong M, Gusella V. Dynamic response of masonry arch with geometrical irregularities subjected to a pulse-type ground motion. Nonlinear Dyn 2018;91(1):609–24. https://doi.org/10.1007/s11071-017-3897-z. ⟨https://www.scopus.com/inward/record.uri?eid=2-s2.0-85032792785&doi=10.1007%2fs11071-017-3897-z&partnerID=40&md5=c50d6f12ddb149cba3ac721f6f16f7e9⟩.
[35] Augusthus-Nelson L, Swift G. Experimental investigation of the residual behaviour of damaged masonry arch structures. Structures 2020;27:2500–12. https://doi.org/10.1016/j.istruc.2020.08.008. ⟨https://www.scopus.com/inward/record.uri?eid=2-s2.0-85090051358&doi=10.1016%2fj.istruc.2020.08.008&partnerID=40&md5=26152b474af222f1804953df624df61e⟩.
[36] Zampieri P, Cavalagli N, Gusella V, Pellegrino C. Collapse displacements of masonry arch with geometrical uncertainties on spreading supports. Comput Struct 2018;208(19). https://doi.org/10.1016/j.compstruc.2018.07.001.
[37] Augusthus-Nelson L, Swift G. Experimental investigation of the residual behaviour of damaged masonry arch structures. Structures 2020;27:2500–12. https://doi.org/10.1016/j.istruc.2020.08.008. ⟨https://www.scopus.com/inward/record.uri?eid=2-s2.0-85090051358&doi=10.1016%2fj.istruc.2020.08.008&partnerID=40&md5=26152b474af222f1804953df624df61e⟩.
[38] Durm, J. Handbuch der Architektur (Theil 2, Die Baustile; Bd. 2): Die Baukunst der Etrusker, die Baukunst der Römer Darmstadt, 1885 https://doi.org/10.11588/diglit.2021.
[39] Huerta DS. Galileo was Wrong: The Geometrical Design of Masonry Arches. 25-521590-5896/06/020025-28 Nexus Netw J 2006;8. https://doi.org/10.1007/s00004-006-0016-8.
[40] Milani, G., Sarhosis, V. From corbel arches to double curvature vaults: Analysis, conservation and restoration of masonry structures of architectural heritage. (2022). Springer, Research for Development. DOI: https://doi.org/10.1007/978–3-031–12873-8_1.
[41] MATLAB - Version 9.9.0 (R2020b), Natick, Massachusetts: The MathWorks Inc., 2020.
[42] Milani, G. Limit analysis of masonry arches: a primer on computational approaches based on linear programming, Como, Italy: Lesson slides from summer school "From Corbel Arches To Double Curvature Vaults: Data Acquisition, Structural Analysis, Conservation And Restoration Of Architectural Heritage Masonry", 2021.
[43] Dantzing G, Orden A, Wolfe P. Generalized simplex method for minimizing a linear form under linear inequality restraints. Pac J Math 1955;vol. 5:183–95.
[44] Mehrotra S. On the implementation of a primal-dual interior point method. SIAM J Optim 1992;vol. 2:576–601.
[45] Zhang, Y., Solving large-scale linear programs by interior-point methods under the MATLAB environment in Technical Report TR96–01, Department of Mathematics and Statistics, University of Maryland, Baltimore County, Baltimore, MD, 1995.
[46] RDF, CIRCE - IUAV Università degli Studi di Venezia, 1999.